Numerical Investigation of the Dynamic Characteristics of a Dual-Throat-Nozzle for Fluidic Thrust-Vectoring

AIAA JOURNAL
Vol. 55, No. 1, January 2017

Numerical Investigation of the Dynamic Characteristics of a Dual-Throat-Nozzle for Fluidic Thrust-Vectoring

Michele Ferlauto* and Roberto Marsilio†
Politecnico di Torino, 10129 Turin, Italy

DOI: 10.2514/1.J055044

A computational method tailored for the simulation of fluidic thrust-vectoring systems is employed to investigate the dynamic response of a dual-throat nozzle in open- and closed-loop control. Thrust vectoring in fixed, symmetric nozzles is obtained by secondary flow injections that cause local flow separations, asymmetric pressure distributions, and, as a consequence, the vectoring of primary jet flow. The computational technique is based on a well-assessed mathematical model for the compressible unsteady Reynolds-averaged Navier–Stokes equations. A minimal control system governs the unsteady blowing. Nozzle performances and thrust-vector angles have been computed for a wide range of nozzle pressure ratios and secondary flow injection rates. The numerical results are compared with the experimental data available in the open literature. Several computations of the open-loop dynamics of the nozzle under different forcing have been performed to investigate the system response in terms of thrust-vectoring effectiveness and controllability. These computations have been used to extract autoregressive exogenous models of the nozzle dynamics. The effects of including the actuator dynamics are also discussed. Simple strategies of closed-loop control of the nozzle system by proportional–integrative–derivative regulators are investigated numerically. The closed-loop model predictive control of the system, based on the autoregressive exogenous models, is addressed.

Nomenclature

C_d	=	$(w_s + w_p)/w_{i,p}$, discharge coefficient of primary nozzle
$C_{f,g_{sys}}$	=	$(F_A + F_N)/(F_{i,p} + F_{i,s})$, system resultant thrust ratio
F_A	=	nozzle axial force
F_N	=	nozzle normal force
j	=	1, 2; injection slot number
MFR	=	$w_s/(w_s + w_p) \cdot 100$, mass flow ratio
NPR	=	nozzle pressure ratio
P	=	static pressure
P^o	=	total pressure
u	=	control variable
w	=	mass flow rate
$w_{i,p}$	=	ideal mass flow rate of primary nozzle
δ	=	$\tan^{-1}(F_N/F_A)$, pitch thrust-vector angle
η	=	δ/MFR, thrust-vectoring efficiency

Subscripts

i	=	ideal
p	=	primary
s	=	secondary
1, lw	=	lower injection slot
2, up	=	upper injection slot

I. Introduction

THRUST vectoring represents for the aircraft system an additional control variable that offers many benefits in terms of maneuverability and control effectiveness [1–3]. For instance, actual multi-axis thrust-vectoring technology based on movable nozzles allows unconventional maneuvers such as the "helicopter J-turn backflip" or the acrobatic "hammerhead" safely, even if the aircraft is in stalled conditions for the main part of the maneuver. Thrust vectoring helps vehicles meet takeoff and landing requirements, and it can be a valuable control effector at low dynamic pressures, where traditional aerodynamic controls are less effective [4–7]. Advantages are also expected for supersonic aircraft, where the use of thrust-vectoring nozzles with a canard airframe configuration can allow for lower sonic-boom signatures than possible with conventional configurations [6]. Additionally, thrust vectoring could increase conventional controls for some control power to trim the aircraft and thus reduce cruise trim drag [8].

Fluidic thrust vectoring (FTV) retains the advantages of mechanical thrust vectoring without the need of the complex adjustable hardware of the variable geometry devices [9]. FTV strategies follow the principle of flow manipulation to obtain a lateral force on a nozzle of fixed geometry. In general, the effect is obtained by injecting into the nozzle a secondary flow of bleed air. The injected fluid interacts with the exhaust flow into the fixed nozzle, and by breaking the symmetry, it generates an asymmetric flowfield and wall pressure distributions that give rise to a side component of the thrust vector. The FTV technology does not increase significantly the aircraft weight, and it can be applied to systems that were not originally designed with such a feature. The key point for the fluidic approach is to identify a manipulation technique that can gradually modulate the symmetry-breaking effect within an acceptable range of deterioration of the nozzle performances. The most effective techniques that have been studied in literature include shock vector control, counterflows, throat shifting, and supersonic dual-throat nozzle. The performances of these approaches have been measured in terms of control efficiency and thrust loss. The efficiency of vectoring is computed as the degree of vectoring achieved per percent of secondary flow required as compared to the primary nozzle flow. Briefly, the shock vector control method works by generating a shock system that makes the nozzle flow asymmetric. The shock system is effective at turning the flow, but at the consequence of total thrust [4,10]. The counterflow method uses suction between the trailing edge of the nozzle and an aft collar. The suction creates a reversed flow along the collar, which causes a pressure drop and an increase in velocity near the reversed flow area, thus providing a thrust differential [4]. As a drawback, an additional equipment to provide the suction is required. The fluidic throat-shifting method uses jets of secondary flow to create a new effective geometry at the throat and to turn the flow while it is still subsonic. It has minimal thrust losses but also suffers from low performance [4,9]. Better performances are achieved when throat shifting is applied to the dual-throat nozzle (DTN) concept. This nozzle has two minimum throat areas with a

Received 20 January 2016; revision received 5 June 2016; accepted for publication 16 August 2016; published online Open Access 3 November 2016.

*Aggregate Professor, Department of Mechanical and Aerospace Engineering, Corso Duca Degli Abruzzi 24. Member AIAA.

†Associate Professor, Department of Mechanical and Aerospace Engineering, Corso Duca Degli Abruzzi 24.

recessed cavity positioned in between. When a secondary flow is injected at the upstream throat, it causes the flow separation and a skewing effect. In the recirculation zone generated by the flow separation, a low-pressure plateau is observed, whereas the blockage effect induced by this cavity flow promotes the flow reattachment on the opposite wall. The combination of these two effects provides additional vectoring. The optimal design and the static performances of this nozzle concept have been investigated both experimentally and numerically at NASA Langley Research Center (NASA LaRC) [4–7,11] for both the two-dimensional and axisymmetric configurations. The DTN-tested geometries had nozzle expansion ratios optimized for operating conditions corresponding to takeoff and landing, midclimb, and cruise. According to Flamm et al. [11], the best thrust-vectoring performance is obtained when the two minimum areas are equal. Recently, other numerical and experimental investigations [12–14] have been performed, and new DTN optimal geometries have been suggested.

Secondary flow injection has been also used to investigate the thrust-vectoring control on a cold-flow aerospike nozzle [15]. Another approach of jet vectoring is based on the use of synthetic jets instead of continuous blowing [16] and on plasma actuators [17].

Until now, the FTV research has focused on the study of efficient flow manipulation strategies (i.e., on how to deflect the flow with lowest energy external forcing). As a consequence, the nozzle performances at steady-state conditions have been mainly investigated. The experimental testing of a DTN dynamics is undergoing research [18].

Because all the flow manipulations mentioned previously introduce strong nonlinearities in the flow (e.g., shocks, separations, recirculating flows), the dynamic response of the nozzle system and the possible control strategies must be investigated to obtain a reliable thrust vectoring. Unsteady computational fluid dynamics (CFD) analyses can help in deriving the time-varying nozzle performances, in clarifying the role and interaction between various nonlinear phenomena, and in assessing and testing the open/closed-loop control. This is even more stringent when fully unsteady manipulators are used (e.g., synthetic jet actuators). For this purpose, a numerical framework for the unsteady simulation of the vectoring nozzle in open- and closed-loop conditions has been developed [19]. The method is applicable to all the FTV strategies mentioned previously.

In the present paper, the dynamic characteristic of the DTN tested at NASA LaRC [7] is studied. This nozzle geometry has been selected as a reference because of the wider availability of experimental and numerical data. The nozzle configuration has been modified by adding a second injection point on the upper boundary, as shown in Fig. 1. This allows for a full excursion of the exhaust flow either upward or downward. The system dynamics has been investigated numerically by simulating the response to various inputs. Both open-loop and closed-loop transient evolution have been computed. Autoregressive exogenous (ARX) models of the fluidic system dynamics have been derived by using system identification techniques. These lower-order models have been used to extract the essential part of the system dynamics and to attempt preliminary tests of model-based predictive control.

The presentation of the work is as follows. In the next section, the nozzle setup as well as the open- and closed-loop schemes are described. Then, the mathematical model and the numerical approach are explained. The procedure is validated against numerical and experimental data available in the open literature, and results about the open-loop and closed-loop transient evolution of the nozzle flow are presented. The influence of the actuator dynamics is also discussed. Finally, a procedure of identifying an optimal ARX model of the nozzle dynamics is illustrated, and its application to model-based predictive control is tested.

II. Nozzle System Setup and Control

A general sketch of the DTN geometry is illustrated in Fig. 1. With respect to the test rig of [11], an additional flow ejector has been placed in the upper boundary, thus allowing the nozzle to deflect the

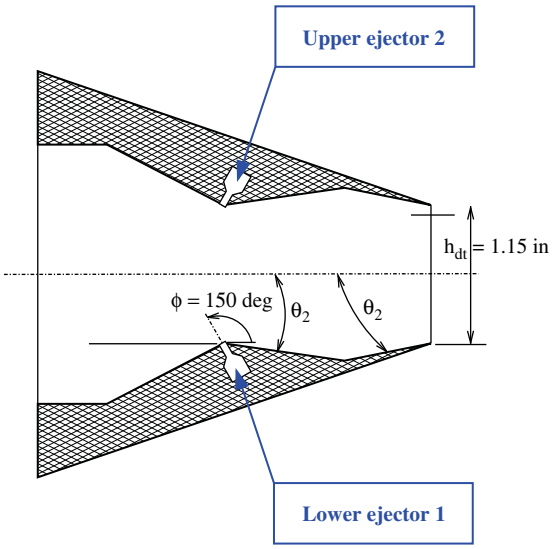

Fig. 1 Dual-throat nozzle geometry and flow actuators location.

exhaust flow upward. The flow manipulation is handled by the ejector activation scheme outlined in Fig. 2. This sketch can be also interpreted as a scheme of the open-loop control of the nozzle, and it is applicable to other FTV approaches. In case of blowing, the secondary flow apparatus can be fed by the engine compression system (e.g., by the high-pressure compressor), which also dictates the total conditions of the injected flow. Then, the secondary mass flow rate is modulated by an actuation valve, which causes a total pressure drop in the fluidic system. Either the pressure drop or the total pressure level of the injected flow can be adopted as the control variable of the nozzle system.

As mentioned, the two-dimensional (2-D) nozzle is endowed with an injection point on the lower boundary and a second one on the upper boundary. We assume a mutually exclusive control logic for the blowing action, that is, only one actuator can be active at a time. This assumption simplifies the description of the control law because the control action can be represented by a single variable by merging the input signals as shown in Fig. 3. We define the control variable $u(t)$ as follows:

$$u(t,j) = P_2^o(t)\cdot(j-1)\cdot[P_2^o(t) > P_{e2}(t)] + P_1^o(t)\cdot(j-2)\cdot[P_1^o(t) > P_{e1}(t)] \tag{1}$$

where the terms in brackets are logical expressions with true $= 1$, false $= 0$; and P_{e1}, P_{e2} are the time-dependent static pressures at the ejector exit. Reverse flow inside the ejector is not allowed. The same logic can be expressed as a function of the pressure drops $\Delta P_j = P_j^o(t) - P_{ej}(t)$, but still one has to ensure $\Delta P_j \geq 0$, as

$$u(t,j) = \max\{P_2^o(t) - P_{e2}(t), 0\}\cdot(j-1) + \max\{P_1^o(t) - P_{e1}(t), 0\}\cdot(j-2) \tag{2}$$

By following the proposed logic, the absolute value of the control is applied as total pressure level either to the lower ejector, if $u < 0$, or to the upper ejector, if $u > 0$. No action is applied if $u = 0$ or when the imposed total pressure would cause reverse flow in the secondary system.

For convenience, some output signals (e.g., the secondary mass flow w_s) are built up following the same rule of the input, that is, negative values refer to the lower secondary jet, positive to the upper:

$$w_s(t,j) = w_2(t)\cdot(j-1) + w_1(t)\cdot(j-2) \tag{3}$$

This allows us to reduce the nozzle to a single-input/single-output system. The control and the response can be represented by two scalar

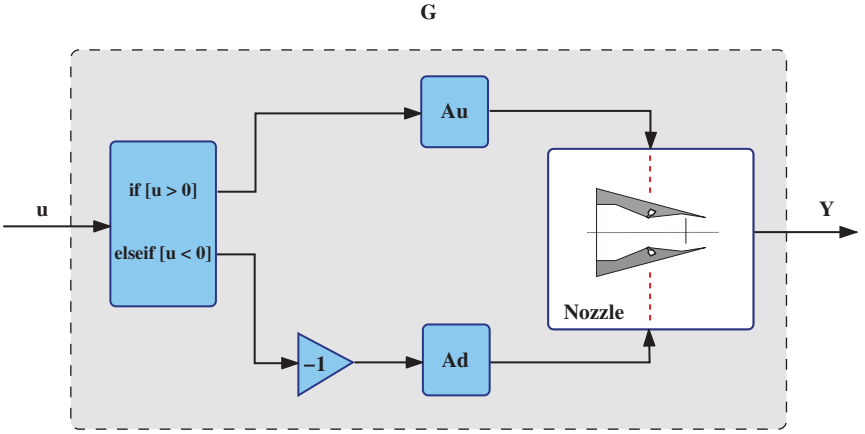

Fig. 2 Open-loop control of the nozzle system. A_u, A_d are the transfer functions of the upper and lower actuator, respectively.

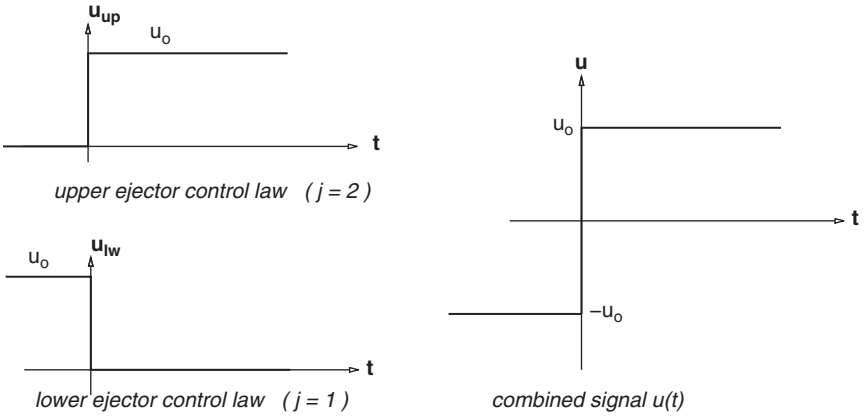

Fig. 3 Merging of the two input signals for actuators 1 and 2 in a single control variable $u(t)$.

variables drawn in a single 2-D plot. Conversely, from the combined function $f(t)$ (i.e., P_j^o or w_s), one can deduce the contribution from the two actuators as

$$f_1 = |f| \cdot [f < 0], \qquad f_2 = |f| \cdot [f > 0] \tag{4}$$

that is, the absolute value of the synthetic signal $f(t)$ gives us the intensity, whereas the sign refers to the actuator.

III. Mathematical Model

The main flowfield is simulated by using a finite volume discretization of the compressible unsteady Reynolds-averaged Navier–Stokes (URANS) equations. The one-equation model of Spalart–Allmaras (SA) [20] is used for the turbulence modeling. The set of governing equations are written in the compact integral form:

$$\frac{\partial}{\partial t}\int_v \boldsymbol{W}\,\mathrm{d}\mathcal{V} + \int_{\mathcal{S}} \boldsymbol{F}_I \cdot \hat{n}\,\mathrm{d}\mathcal{S} + \int_{\mathcal{S}} \boldsymbol{F}_V \cdot \hat{n}\,\mathrm{d}\mathcal{S} = \int_{\mathcal{V}} \boldsymbol{H}\,\mathrm{d}V \tag{5}$$

where $\mathcal{V}$ represents an arbitrary volume enclosed in a surface $\mathcal{S}$. $\boldsymbol{W}$ is the hypervector of conservative variables; $\boldsymbol{F}_I$ and $\boldsymbol{F}_V$ are tensors containing the inviscid and the viscous fluxes, respectively:

$$\begin{aligned}
\boldsymbol{W} &= \{\rho, \rho\boldsymbol{q}, E, \tilde{\nu}_t\}^T \\
\boldsymbol{F}_I &= \left\{\rho\boldsymbol{q}, p\bar{\bar{I}} + \rho\boldsymbol{q}\otimes\boldsymbol{q}, (E+p)\boldsymbol{q}, \tilde{\nu}_t\boldsymbol{q}\right\}^T \\
\boldsymbol{F}_V &= \frac{\sqrt{\gamma M_\infty}}{Re_\infty}\left\{0, -\bar{\bar{\tau}}, -\kappa\nabla T - \bar{\bar{\tau}}\cdot\boldsymbol{q}, -\frac{\nu+\tilde{\nu}_t}{\sigma}\nabla\tilde{\nu}_t\right\}^T
\end{aligned} \tag{6}$$

$\boldsymbol{q} = \{u, v, w\}^T$ is the velocity vector; E is the total energy per unit volume; M_∞ and Re_∞ are the freestream Mach number and the Reynolds number; γ is the ratio of the specific heats; and finally, $\bar{\bar{I}}$ is the unit matrix. The nonhomogeneous term $\boldsymbol{H}$ is due to the turbulence model:

$$\boldsymbol{H} = \left\{0, 0, 0, c_{b1}\tilde{S}\tilde{\nu}_t + \frac{c_{b2}}{\sigma}(\nabla\tilde{\nu}_t)^2 - c_{w1}f_w\left(\frac{\tilde{\nu}_t}{d}\right)^2\right\}^T \tag{7}$$

Turbulent eddy viscosity $\tilde{\nu}_t$ apart, $\boldsymbol{H}$ contains turbulence model constants and parameters. The reader is referred to [20] for a full explanation of the model and constants. System (5) is nondimensionalized with respect to the reference length L, to freestream density ρ_∞, temperature T_∞, and viscosity μ_∞. The reference velocity and time are $\sqrt{\mathcal{R}T_\infty}$ and $L/\sqrt{\mathcal{R}T_\infty}$, respectively. The viscous stresses are written as

$$\tau_{ij} = (\mu + \mu_t)\left[\frac{\partial q_j}{\partial x_i} + \frac{\partial q_i}{\partial x_j} - \frac{2}{3}(\nabla\cdot\boldsymbol{q})\delta_{ij}\right] \tag{8}$$

where the laminar viscosity μ is computed via Sutherland's law. The turbulent viscosity $\mu_t = \rho\nu_t$ is computed through the Spalart–Allmaras one-equation turbulence model [20,21]. Despite its simplicity, the SA model has shown a closer agreement with the experimental data for the case of unsteady or pulsatile flow when compared to $k-\epsilon$ and $k-\omega$ shear-stress transport models [22,23].

The numerical solution of system (5) is based on a Godunov method with flux-difference splitting and an essentially non-oscillatory scheme second-order accurate in both time and space. The integration in time is carried out according to a fourth-order Runge–Kutta scheme. Further numerical details, as well as the code validation, can be found in [24]. The numerical method has been efficiently parallelized by using OpenMP directives. The spatial and time accuracy of the solver has been widely tested in many unsteady

compressible flowfields as, for instance, the flow manipulation by synthetic jets and poststall control of NACA0015 profile [22]; the simulation of rotating stall generation and evolution [25]; time-dependent flows with moving grids [26,27]; and the computation of aeroelastic standard configurations and blade flutter.

The computational domain is bounded by artificial (i.e., far-field) boundaries and physical contours (i.e., impermeable walls). The boundary condition (BC) enforcement follows the guidelines the characteristic-based approach given in Poinsot and Lele [28] and Ferlauto et al. [29]. The blowing action of the actuators placed on the nozzle walls is simulated by a boundary condition applied to all the grid cells m adjacent to the actuator orifice as well as lying on the boundary of the computational domain. The numerical fluxes on the interface of the generic cell m and the ejector j are computed by solving a Riemann problem. From the knowledge of the state on the cell m and of the mean total conditions inside the ejector j, the flow variables (a^*, u^*, v^*, S^*) at the interface * lying on the boundary are derived by solving the following equation system:

$$a^{*2} + \frac{\gamma - 1}{2} u^{*2}(1 + \tan^2\phi) = \gamma T_j^o \tag{9}$$

$$S^* = \gamma \log T_j^o - (\gamma - 1) \log P_j^o \tag{10}$$

$$a^* \exp\left(\frac{S_m - S^*}{2\gamma}\right) - \frac{\gamma - 1}{2} u^* = \frac{2\gamma}{\gamma - 1} a_m - u_m \tag{11}$$

$$v^* = u^* \tan(\phi) \tag{12}$$

The conditions [Eqs. (9–12)] are a simplification of the suction/blowing model derived in [22] and are similar to the BCs for the flow inlet [28].

IV. Numerical Results

In the next sections, the numerical results obtained are grouped into four classes: the simulation of the static performances of the manipulated nozzle flow; the simulation of the transient dynamics of the system with or without actuator dynamics; the reduced-order modeling of the nozzle dynamics; and some numerical experiments of closed-loop control with proportional regulators or by a model-based predictive controller.

A. Steady-State Validation

The validation of the numerical tool used for the simulations has been addressed in [19] and will be just summarized here. The static performances of the dual-throat nozzle during thrust vectoring have been computed at different rates of secondary flow injection MFR and at different NPRs. The results were compared against experimental and numerical data. Different mesh sizes were also used to check convergence to grid-independent solutions. The reference nozzle geometry for all the simulations was characterized by the parameters $\vartheta_1 = -10$ deg and $\vartheta_2 = 20$ deg (see Fig. 1). The choice of this geometry was motivated by the wider range of experimental data and numerical results available in the open literature. Moreover, the selected DTN configuration was the result of a parametric study that has identified the optimal values of many of the parameters involved in the manipulation (e.g., actuator position, blowing direction, throat area ratio) [5,6].

The results of the steady flow computations were obtained by varying the secondary mass flow rate MFR at NPR $= 4$ are summarized in Fig. 4. The performances of the DTN at fixed blowing rate MFR $= 3\%$ and for different nozzle pressure ratios NPR are displayed in Fig. 5. All the computations have been performed on a 205×121 orthogonal grid shown in Fig. 6. This stretched grid has been obtained by conformal mapping techniques, and its optimality has been checked by a grid refinement study [19]. Convergence is assumed as achieved when the L^2-norm W_2-residual is less than 10^{-8}. In the same figures, the experimental and numerical results of [7,11] are reported for comparison. As visible, the present numerical predictions are in good agreement with the experimental data. The numerical computations of [6] show a higher mismatch that is probably due to the weaker convergence criterion used (i.e., $|\Delta\delta| \leq 0.5$ deg). The pressure distribution at the wall is also well captured by the numerical method. The computed static pressure is compared with the experimental one in Fig. 7. The figure puts also on evidence the recirculation zones (where the pressure is nearly constant), the peak in the blow region and the shock location.

B. Transient Response and System Dynamics

In this section, the evolution of the system subjected to prescribed control inputs is considered. The flow is manipulated by bleeding air at prescribed total conditions (e.g., air extracted from the compression system). The secondary mass flow is modulated by valves, so that the fluid undergoes an isenthalpic process with a variation/loss of total pressure. A minimalistic scheme of the system is depicted in Fig. 2. The input signal $u(t)$ is defined by Eq. (1) and corresponds here to the imposition of a mean total pressure $P_j^o(t)$ in

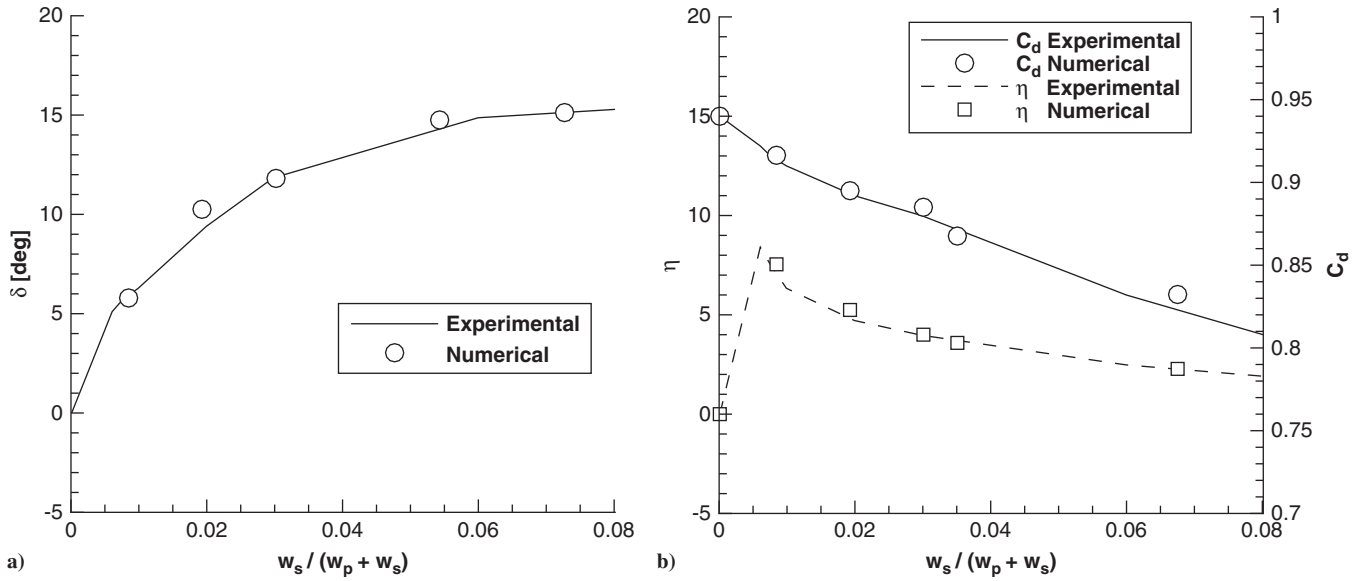

Fig. 4 Comparison of nozzle performances at NPR $= 4$ with experimental data [6]: a) thrust angle; b) discharge coefficient CD and vectoring efficiency η versus secondary mass flow rate MFR $= w_s/(w_s + w_p)$.

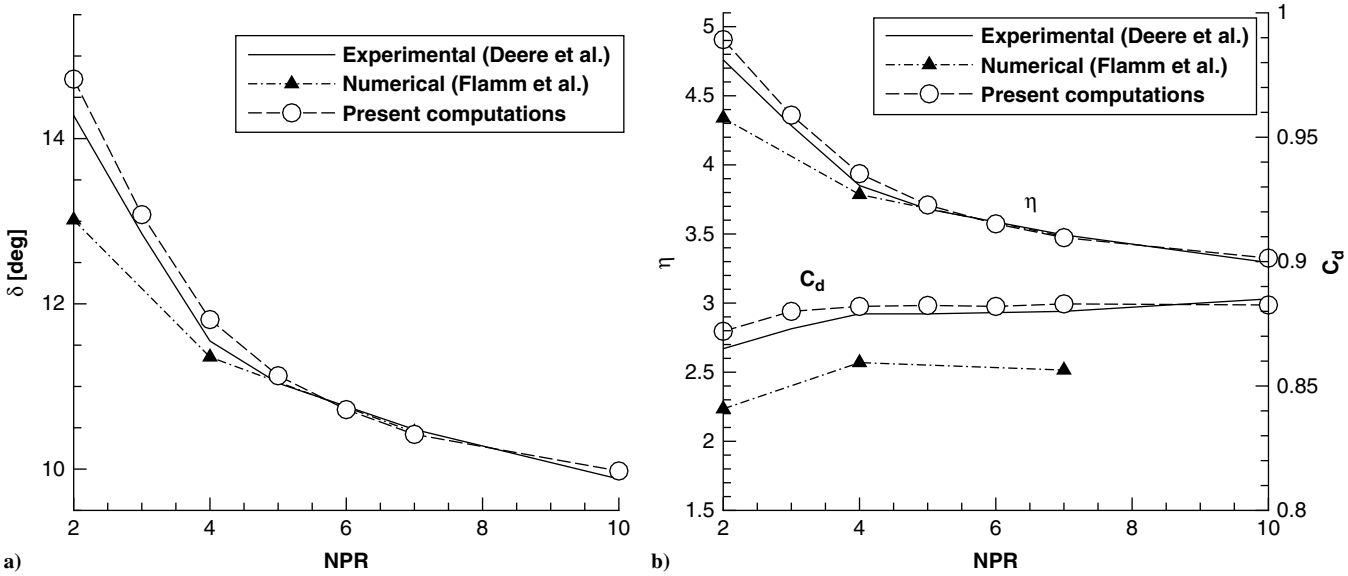

Fig. 5 Comparison of nozzle performances at MFR = 3% with experimental and numerical data [6]: a) thrust angle; b) discharge coefficient CD and vectoring efficiency η versus nozzle pressure ratio NPR.

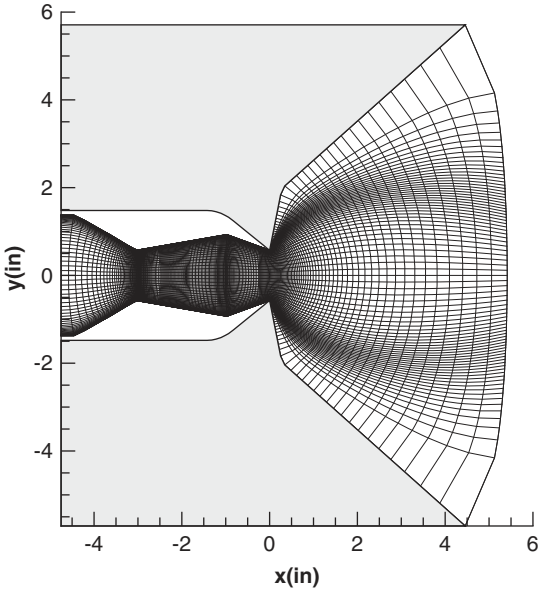

Fig. 6 Computational grid.

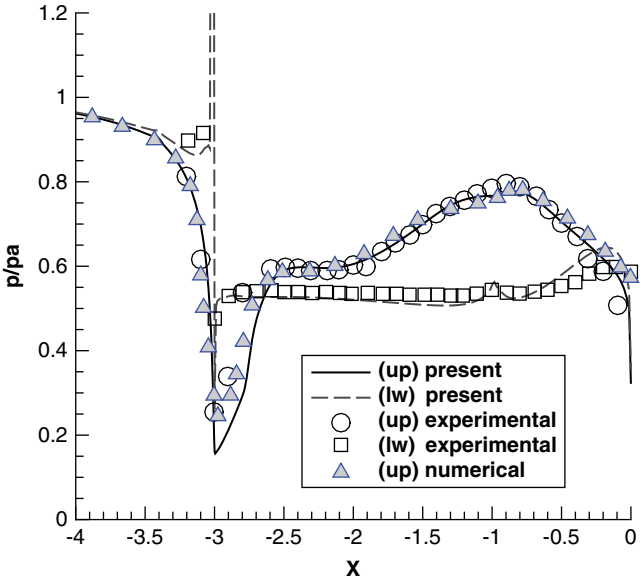

Fig. 7 Comparison of the computed wall pressure distribution at MFR = 3% and NPR = 4 with the experimental and numerical data [6].

the jth ejector, with $j = 1, 2$. The system response is computed by a time accurate integration of the flow governing equations. Several computations have been performed to study the system response to a variety of input pressure profiles and injection laws. A typical transient response of the nozzle system is shown in Figs. 8 and 9. The forcing law $u(t) = P_j^o(t)$ applied and the corresponding unsteady evolution of the thrust angle $\delta(t)$ are presented in Fig. 8. Briefly, as visible in that plot, no forcing is applied at the initial condition, so that $u(0) = P_j^*$ and $\delta(0) = 0$. Blowing from the lower ejector is then activated by a step input. After a strong transient, the system reaches a steady state at about $\delta \simeq 12$ deg, while it is MFR = 3% of secondary blowing from the lower ejector. At the nondimensional time $t = 50$, a new forcing step is applied in the opposite direction, symmetrically. After the transient, the nozzle flow is deflected upward (and symmetrically with respect to previous configuration) with $\delta \simeq 12$ deg and MFR = 3% of blowing from the upper ejector. During both transients and before reaching the target thrust angle, the system exhibits a strongly nonlinear response characterized by a series of intense overshoots and undershoots.

Some snapshots of the transient flowfield inside the nozzle during forcing are presented in Fig. 9. In the initial condition, shown

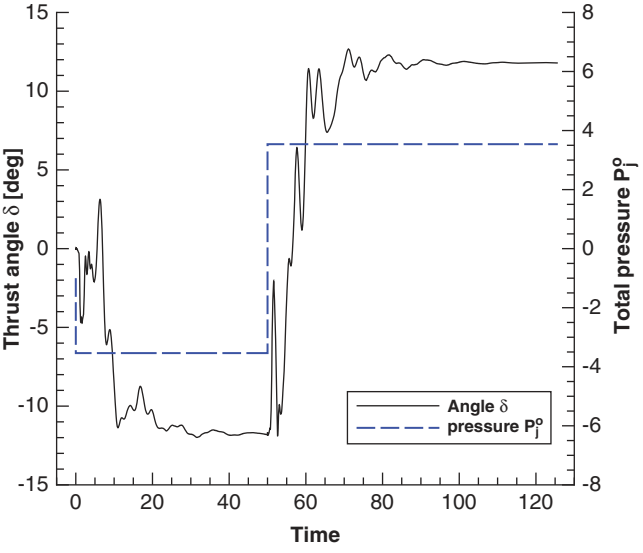

Fig. 8 System response to the input profile.

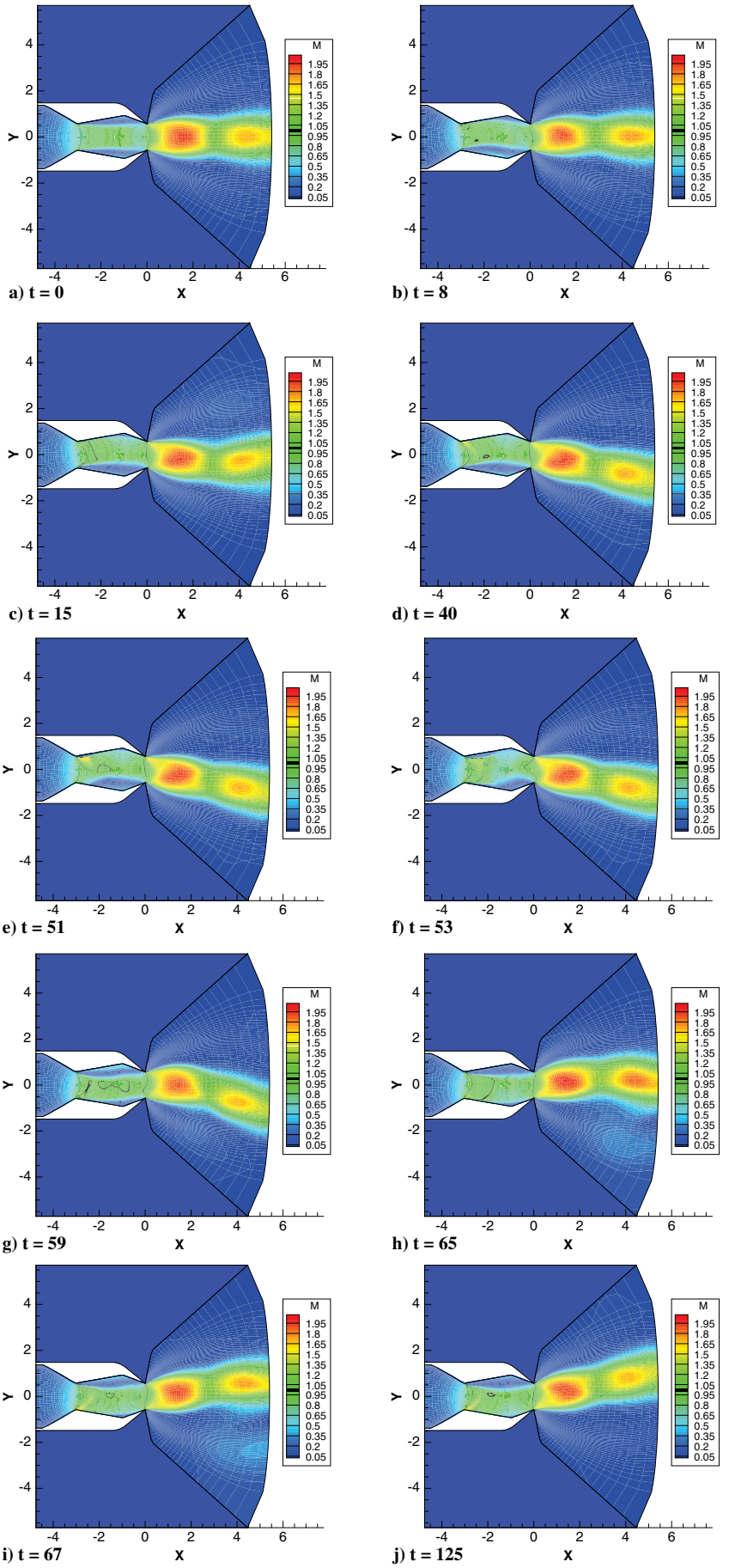

Fig. 9 Transient evolution of the nozzle flowfield in response to the secondary blowing. Mach number contour maps at selected nondimensional time instants.

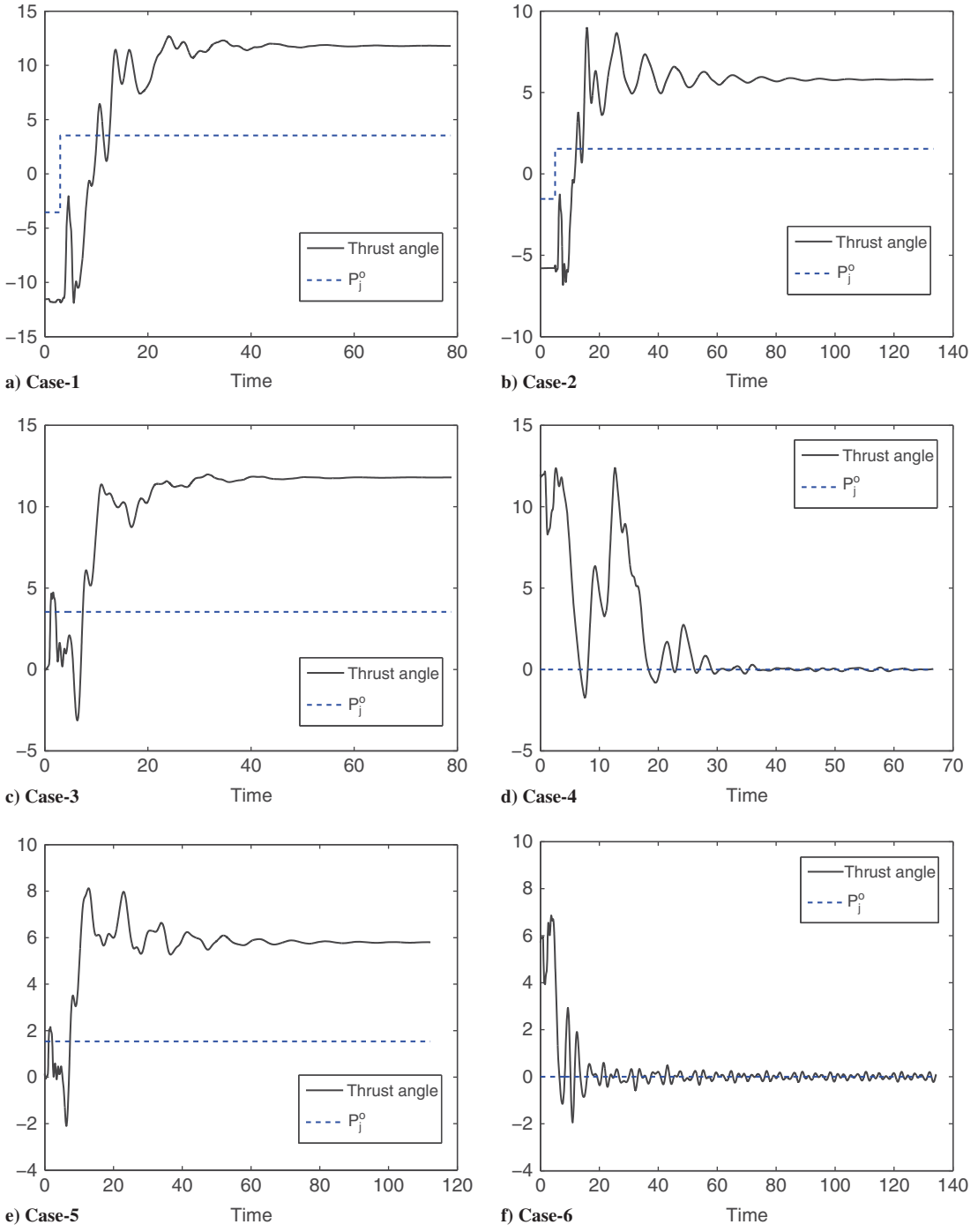

Fig. 10 Response of the nozzle system to selected step forcing of the blowing as defined in Table 2.

in Fig. 9a, the flow is symmetric, and it is expanding between the two recirculation zones located on the cavities formed by the dual-throat geometry. When the secondary blowing is activated, it promotes the one-side separation on the lower boundary before the throat, thus enhancing the lower vortex bubble and virtually modifying the nozzle shape, as visible in Figs. 9b and 9c. The increased blockage effect of the lower vortex promotes the flow reattachment on the upper boundary. Moreover, the flow displacement allows for a stronger expansion on the upper boundary and the flow recompression after the first throat is realized through a moving oblique shock. At time $t = 40$, the system reaches a nearly steady-state condition characterized by a large separation bubble on the lower cavity and a small recirculation zone on the upper wall (Fig. 9d). At time $t = 50$, a second step input generates a new transient presented in Fig. 9. The previous flow pattern is destroyed, and the system adjusts itself to a new steady configuration, which is specular to the previous one.

The choice of a step function as input/forcing is not casual. This is a common practice in the analysis of dynamic systems, in control design, and in system identification. For linear systems, the response of the system to a generic forcing law can be deduced by convolution with the step response (i.e., by Duhamel's integral formula [30,31]). For nonlinear systems, the approach of linearized approximations can be followed.

For this reason, in a second group of simulations, the system is subjected to step forcing of different intensity. Initial and final states of these step inputs are summarized in Tables 1 and 2. From the analysis of the system dynamics, as plotted in Fig. 10, a typical behavior can be observed. The system response exhibits first an overshoot toward the direction impressed by the forcing action.

Table 1 Definition of the actuator setup for each blowing level

State	j	Bleed	MFR	P_j^o	δ, deg
a	2	Up	3.0	3.538	11.8
b	2	Up	0.85	1.538	5.8
c	0	None	0	n.a.	0.0
d	1	lw	0.85	1.538	−5.8
e	1	lw	3.0	3.538	−11.8

Then, an undershoot in the opposite direction follows, leading the system close to the initial condition. After that, the system evolves in the right direction with several damped oscillations, and finally it reaches the new steady state. This behavior can be appreciated either when the system is forced from $\delta = 0$ toward a nonnull value of the thrust angle or when the secondary blowing is ceased and the system relaxes to the symmetric condition. The dynamics can be explained by observing that the DTN flow is dominated by a complex nonlinear interaction between vortical flows, moving shocks, and flow separations. The numerical simulations have evidenced that the major role is played by the unsteady vortex motions on the upper and lower cavities and on the related flow separations, which are responsible for the generation of the nonsymmetric pressure distribution on the nozzle walls.

To better focus on this dynamics, case 4 is studied with detail because of the large overshoots observed in the nozzle response at later times, when the forcing action is ceased. Moreover, with the actuators inactive, the resulting dynamics does not depend on the blowing model used.

The evolution in time of the thrust angle $\delta(t)$ is reported in Fig. 11a, where also some selected time instants have been labeled from 0 to 5. The snapshot at time 0 corresponds to the initial condition (i.e., to state A of Table 1). The related streamline pattern and shock structure are represented in Fig. 11b together with the wall pressure distribution.

After the instantaneous blowoff of actuator 2, a flow reattachment is observed on the upper wall, close to the throat (Fig. 11c). The flow reattachment reduces both the vortical region of the upper cavity and the asymmetry of the wall pressures, so that the thrust angle decreases accordingly. This process is inverted after time 1, when a new vortex is shed at the throat. The flow topology resembles that of time 0, with a large separation that maintains the pressure at the upper wall nearly constant, whereas the shock increases the pressure on the lower wall.

From time 2 to 3, the shed vortex increases its size and pushes downstream both the previous cavity vortex and the shock structure. The increased strength of the shock causes a significant flow detachment on the lower wall. In Fig. 11e, it can be appreciated how the effects of these interactions cancel out the contributions of the asymmetric wall pressure distributions, and this explains the low thrust angle obtained. The increase of the flow detachment on the lower wall pulls back the shock structure toward the throat and reduces it to a vanishing shock. This flow configuration leads again to a highly nonsymmetric wall-pressure distribution, and the thrust angle increases up to $\delta \simeq 12$ deg at time 4 (Fig. 11f). After that, the cavity flows on both upper and lower walls reassess itself, and the system tends toward the symmetric configuration (Fig. 11g) with $\delta \to 0$.

C. Integration with the Actuator Dynamics

From the time histories of the deflection $\delta(t)$ in Fig. 10, we observed that the steady state is reached in about $\Delta t = 30 - 60$ nondimensional temporal units. For the NASA LaRC test rig considered here, this corresponds to a real time of some milliseconds. If we consider an actual nozzle with a reference length L of the order of 1 m, the transient duration would be of about some tenths of seconds. Although the computed dynamics reveals that the system reaches a steady state for a wide range of the secondary blowing ratio, the wide oscillations of the response curves remain a main concern.

By smoothing the input forcing $u(t)$ (e.g., by using a ramp function instead of a step as control), the nozzle response also becomes smoother. In Fig. 12, the system response $\delta(t)$ to a step forcing (case 7) is compared with the response to two different ramps between the same secondary blowing levels, namely cases 8 and 9 defined in Table 2. As visible, the use of this simple smoothing reduces the wide overshoots.

Table 2 Definition of the forcing functions $u(t)$ for each test-case

Case	$u(t)$	Levels
1	Step	$e \to a$
2	Step	$b \to d$
3	Step	$c \to a$
4	Step	$a \to c$
5	Step	$c \to b$
6	Step	$b \to c$
7	Step	$b \to a$
8	Ramp ($\Delta t = 20$)[a]	$b \to a$
9	Ramp ($\Delta t = 10$)[a]	$b \to a$

[a]Δt is the time interval during which $u(t)$ increases linearly from one state to the other.

It could be also foreseen that, in real hardware systems, the smoothing is somehow introduced by the delayed response of the actuation system.

Let us consider, for instance, a simple bleed valve model based on a transfer function of the form $A_d(s) = A_u(s) = 1/(\tau s + 1)$, where τ is a time constant. The nozzle response with the proposed valve dynamics is shown in Fig. 12 for comparison with the inputs mentioned previously. The selected nondimensional value of $\tau = 4.89$ leads to an actual time constant τ_m for the nozzle test rig of 2 ms, a typical opening value of a bleed valve actuator. Results are comparable to the response curve of case 9.

The smoothing effect of the actuator is weaker if the flow forcing starts from the unmanipulated, symmetric configuration. As an example, case 3 is compared with the nozzle response for two different bleed valve dynamics in Fig. 13. The initial overshots can be motivated by the transition between two very different flow patterns. The previous case 7 develops instead between two manipulated configurations, so that a smoother reassessment of the vortex and shock structure is involved in.

Open- and closed-loop control logics as well as the actuator and sensor dynamics can be simulated within the present CFD tool, and this feature is helpful in testing preformed control laws. Nevertheless, it must be noted that this practice leads to less general results. By including the actuator dynamics, the model loses its generality for two reasons: results are not scalable anymore, and the system response becomes actuator-dependent. For instance, the introduction of the additional time constant τ restricts the fluid dynamic similitude to nozzle flows with

$$\frac{\tau_m}{(L_{\text{ref}}/\sqrt{\mathcal{R}T_{\text{ref}}})_m} = \frac{\tau_n}{(L_{\text{ref}}/\sqrt{\mathcal{R}T_{\text{ref}}})_n} = \tau \tag{13}$$

where the subscript m stands for "model" and n for the actual nozzle. Moreover, the actuator dynamics masks the "raw" dynamics of the nozzle system. In the design process, instead, simplified models of the nozzle dynamics are needed to derive the control logic and to check stability. A dynamic model derived from the CFD computations of the raw nozzle flow ensures that the fluid dynamic similitude holds. The dynamic response predicted by the model can be therefore projected into nozzles of any size that can be coupled with any kind of actuator. Based on these considerations, the replacement of the system in the control chain by reduced-order models of the raw nozzle dynamics seems more appealing.

D. Reduced-Order Modeling of the Nozzle Dynamics

Lower-order models allow for the real-time simulation of the system within a reasonable computational time, and they give

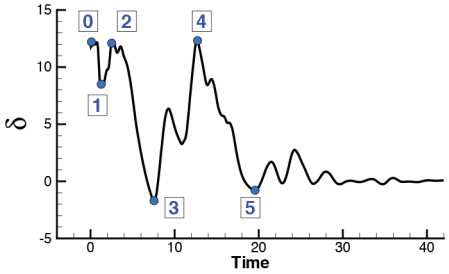

a) Time history of the thrust angle δ. Selected instants are labeled as time 0,1, . . . ,5

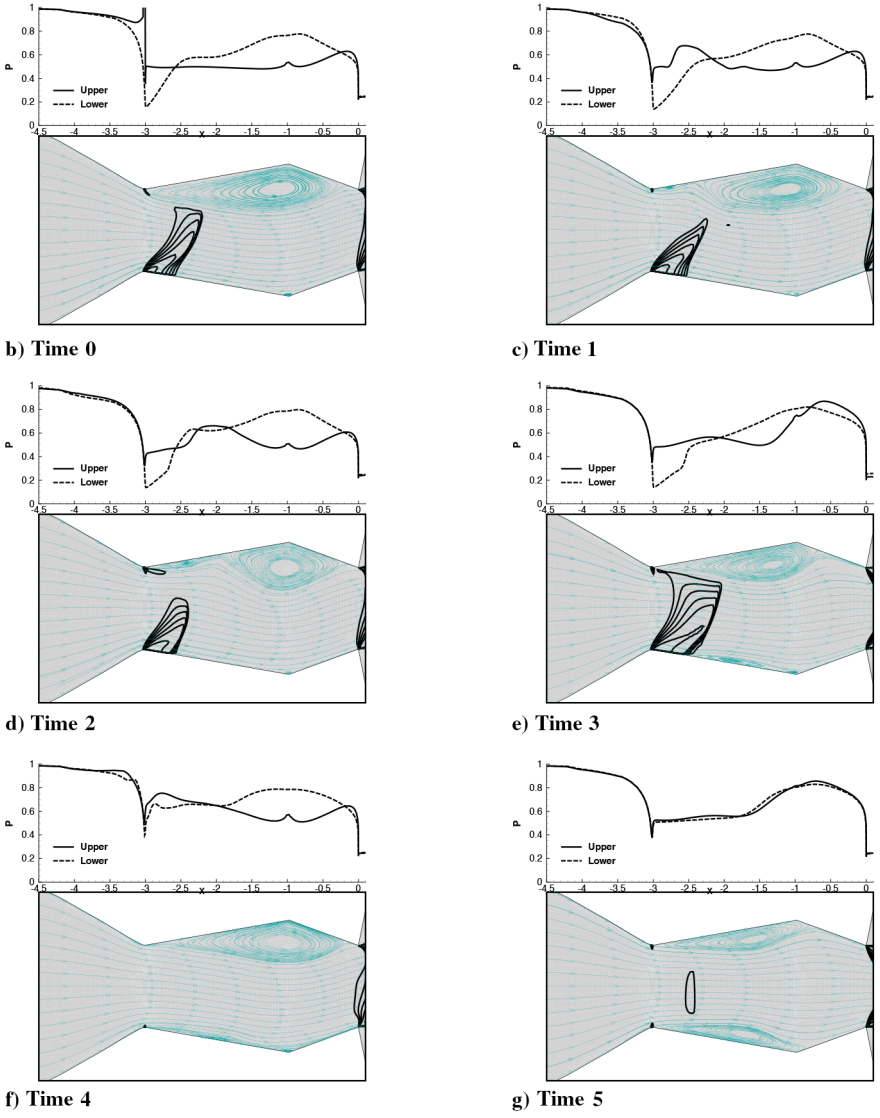

b) Time 0 c) Time 1

d) Time 2 e) Time 3

f) Time 4 g) Time 5

Fig. 11 Nozzle response in Case-4: a) thrust-angle time-history with selected instants, and b–g) snapshots of the wall-pressure distribution, Mach number contours, and streamlines at the selected time instants.

substantial advantages in deriving and testing control algorithms. Standard system identification techniques are employed here to produce a linear model of the nozzle flow dynamics. A set of linear autoregressive exogenous (ARX) models is developed from the numerical simulations of the flow in open-loop conditions listed in Table 2. In the ARX formulation, a linear difference equation relates the input and output as

$$y(t) = -\sum_{i=1}^{n_a} a_i y(t-i) - \sum_{i=1}^{n_b} b_i u(t-i-n_k) + e(t) \qquad (14)$$

where $e(t)$ is the Gaussian noise function; a_k, b_k are the model parameters; and n_a, n_b indicate the order of the $y(t)$ and $u(t)$ polynomials, respectively. The parameter n_k is the time delay between $y(t)$ and $u(t)$. Relation (14) is written in compact form as

$$A(q)y(t) = B(q)u(t-n_k) + e(t) \qquad (15)$$

where

$$A(q) = 1 + a_1 q^{-1} + \ldots + a_{n_a} q^{-n_a} \qquad (16)$$

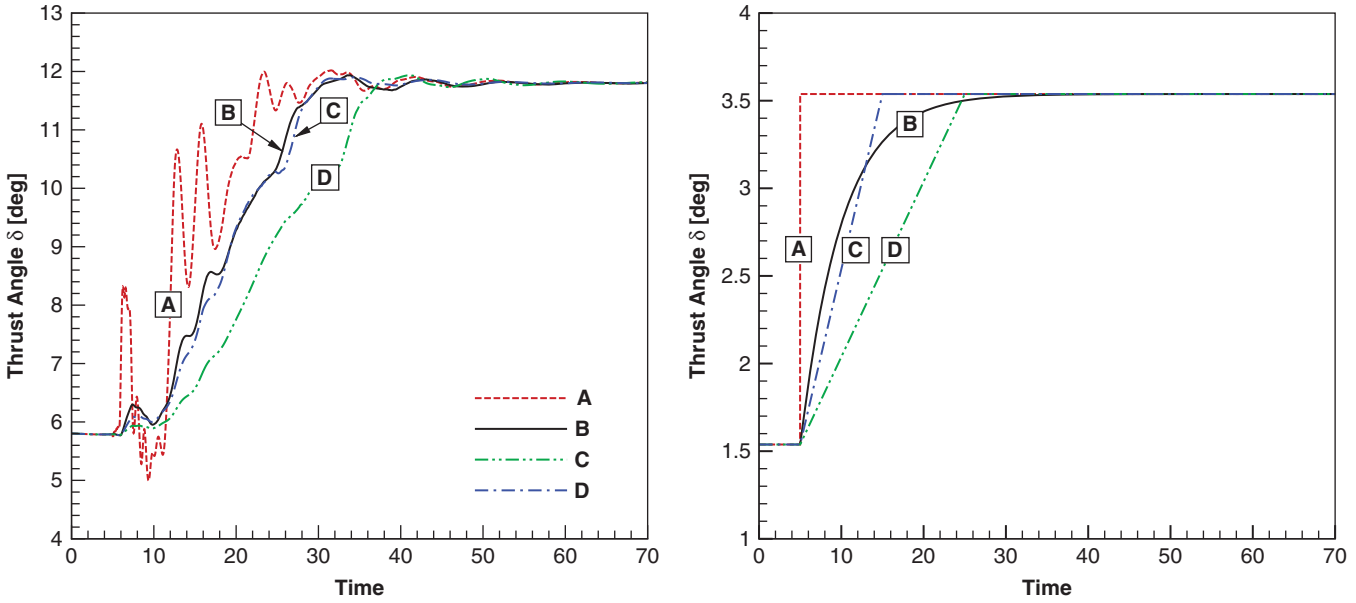

Fig. 12 The nozzle system responses (left) to selected forcing functions (right). Curves are labeled as follows: A = Case-7; B = Case-7 with actuator dynamics ($\tau = 4.89$); C = Case-9 ($\Delta t = 10$); D = Case-8 ($\Delta t = 20$).

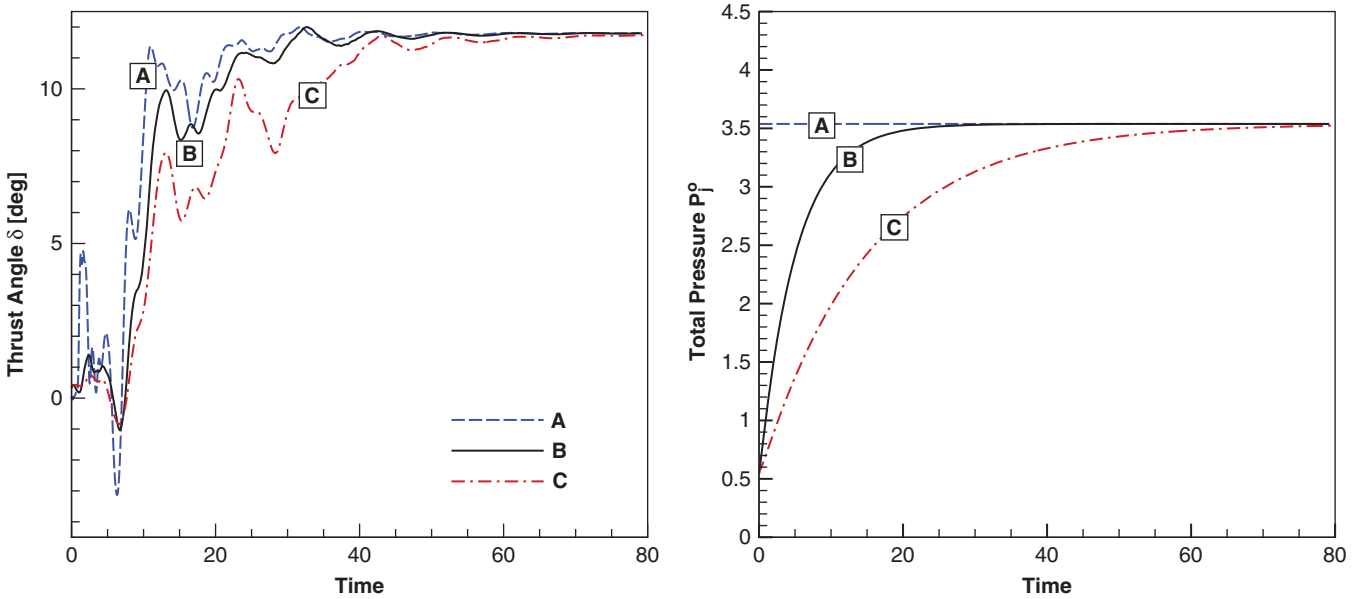

Fig. 13 Comparison of the nozzle response to the step input of Case-3 with different actuator dynamics: a) $\tau = 0$, b) $\tau = 4.89$, and c) $\tau = 14.66$.

$$B(q) = b_1 q^{-1-n_k} + \ldots + b_{n_b} q^{-n_b-n_k} \tag{17}$$

and q^{-1} is the delay operator such as $u(t-1) = q^{-1}u(t)$. The measure of the fit quality $0 \le I_q \le 100\%$ is based on the analysis of prediction error and of the output variance:

$$I_q = 100 \cdot \left(1 - \frac{\|y - \hat{y}\|}{\|y - \bar{y}\|}\right) \tag{18}$$

where $\hat{y}$ is the model-predicted output, and $\bar{y}$ is the mean of the measured output y. The model coefficients a_k, b_k are derived by system identification. From each time series of the system response to prescribed forcing, a minimization of the least-squares parameter residuals is performed [30]. The choice of the coefficient number n_a, n_b, n_k to be used in the process is arbitrary. A parametric study has been carried out to reduce the model to a minimal set of coefficients. The numbers of the model parameters are varied in a wide range. The identification problem is solved for each triplet (n_a, n_b, n_k), and the merit function I_q is computed. The parameter set that describes the ARX model having the best accuracy and the lower order has been selected as optimal. An example of parametric search for case 5 is shown in Fig. 14, where the surface $[I_q(n_a n_b)]_{\max}$, $\forall\ n_k \le 15$ is plotted. The coefficients of the corresponding best-fit and minimal ARX model are summarized in Table 3. The comparison between the model-predicted dynamics and the original CFD data is shown in Fig. 15. The value of I_q is 77.21%.

E. Considerations About the Open- and Closed-Loop Control

The numerical analyses carried out in previous sections concern both the study of the system dynamics and the open-loop control. In fact, the scheme of Fig. 2 that we presented as a way to drive the system is the scheme of an open-loop control. Further investigations toward the design of the control system are outside the present study and will be addressed elsewhere.

We focused, instead, on the simulation of the nozzle system under closed-loop control. A possible strategy for control system design is: 1) derive linear models; 2) use these models to design the controller

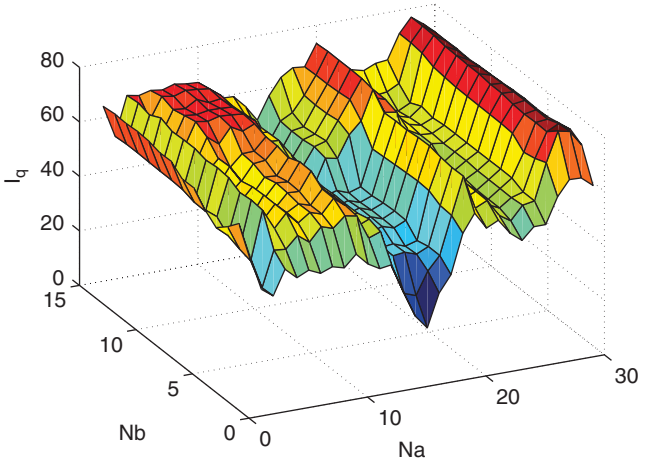

Fig. 14 Parametric search of the best-fit ARX model. The surface represents the function $I_q(n_a,n_b)$ for Case-5.

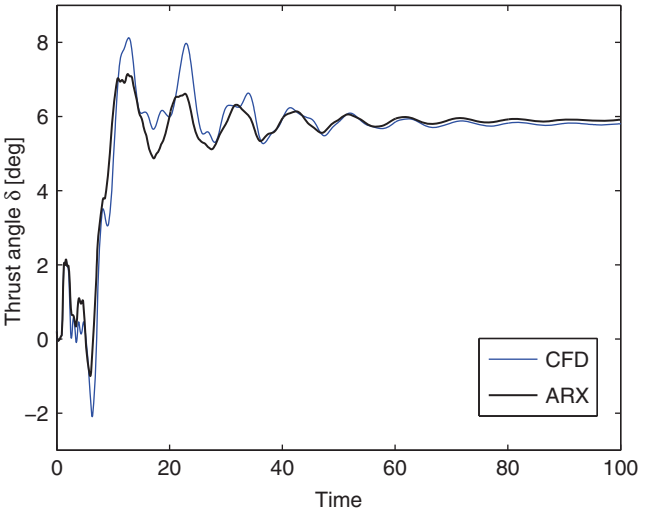

Fig. 15 Best-fit ARX model compared with the original CFD results (Case-5).

by classical methods (e.g., root locus or frequency-domain analysis); and 3) test the controller in the full CFD framework.

As a preliminary step, the computations of the nonlinear system response in closed loop can give the designer more information about the system sensitivity to the controls. For this purpose, some numerical tests have been carried out. The closed-loop controller was derived from simple rules based on semi-empirical methods [32].

A sketch of the nozzle system in closed-loop control is represented in Fig. 17. The block G is the system of Fig. 2. The block R is a general model of a regulator. Typically, R is a proportional–integrative–derivative (PID) controller. In the same figure, the results of a simulation of the closed-loop dynamic response of the nozzle system is shown. The selected objective function is the secondary flow ratio MFR. The parameters of the PID controller have been deduced by using the ultimate cycle approach [32]. As shown in Fig. 16, the target blowing rate is reached very rapidly after the step forcing in $Y^* = \mathrm{MFR}_{\mathrm{req}}$ is activated. The same is true for the pressure level $P_j^o(t)$. The thrust angle δ, instead, still exhibits large variations.

Several numerical attempts of controlling the thrust angle, instead of the MFR, failed. The reason of these failures can be either the simplified approach used in deriving the PID control laws or the inadequacy of a pure PID control strategy in managing a system characterized by strong nonlinearities. We observed that the initial oscillations of the raw nozzle dynamics easily induce the regulator to an excess or weakness of control. The smoother response obtained by including the actuator dynamics does not ensure a successful control in any working conditions. As shown in Figs. 12 and 13, at the early stage, the dynamics still exhibits unwanted oscillations with a temporary inversion of controls, and this condition can be amplified by the proportional control action. This does not infer that PID controllers are ineffective but that the closed-loop control of the thrust angle requires a deeper process of controller design.

Moreover, the final output, e.g., the thrust angle $\delta(t)$, is not a direct consequence of the local flow manipulation, but it comes out from a global flow reassessment. This behavior has been also reported by Flamm et al. [6]. They noted that, although they were attempting to manipulate the angle and location of the sonic line in the nozzle, vectoring the primary flow is not entirely dependent on this manipulation alone. Rather, controlling the flow separation within the recessed cavity was the key to obtaining large vectoring angles. These observations suggest that a more adequate approach to control the DTN thrust vectoring should use more information about the system.

Thrust angle control can be achieved by more advanced closed-loop control techniques as, for instance, the model-based predictive control (MPC) [31], successfully applied, to other nonlinear problems such as the control of separated flows [33]. We derived therefore an MPC control strategy for the DTN system based on the ARX models extracted from the open-loop simulations.

A general scheme of the model predictive controller implemented is illustrated in Fig. 17. The model predictive controller prescribes the intensity of secondary blowing from knowledge of the desired thrust angle and of the actual thrust angle. To determine the blowing law, the model predictive controller uses the linear ARX system model produced by the system identification procedure. Predictions of the resulting thrust angle dynamics are generated using the model for a selected duration into the future (i.e., the prediction horizon) from a sequence of blowing actions over a specified time interval, the control horizon. Optimal values for the new control actions are determined via solution of a quadratic programming problem over the control horizon, such that a cost function involving the deviation from the desired set points is minimized over the prediction horizon [31]. The MPC algorithm can be represented as the optimization problem of minimizing, in the prescribed time horizon, the error between a prescribed system response y and a reference output $w(t)$, or set point, by using a forcing as weaker as possible. A corresponding objective function J is

$$J(N_p,N_u)=\sum_{j}^{N_p}\mu(j)[(\hat{y}(t+j|t)-w(t+j)]^2 + \sum_{j}^{N_u}\lambda(j)[\Delta u(t+j-1)]^2 \tag{19}$$

where N_p is the prediction horizon, N_u is the control horizon, and $\lambda(j)$, $\mu(j)$ are sequences of weights taking into account the future behavior of the system. The problem is generally constrained by

Table 3 Linear ARX model for Case-5

Model: $A(q)y(t)=B(q)u(t)+e(t)$
$A(q)=1-3.7q^{-1}+5.63q^{-2}-4.79q^{-3}+2.86q^{-4}-0.47q^{-5}+0.66q^{-6}-0.19q^{-7}-0.04q^{-8}$ $-0.01q^{-9}+0.25q^{-10}-0.69q^{-11}+1.36q^{-12}-1.83q^{-13}+1.74q^{-14}-1.36q^{-15}+1.28q^{-16}$ $-1.463q^{-17}+1.5q^{-18}-1.31q^{-19}+0.9q^{-20}-0.42q^{-21}+0.09q^{-22}+0.14q^{-23}-0.18q^{-24}$ $+0.07q^{-25}+0.11q^{-26}-0.18q^{-27}+0.08q^{-28}$
$B(q)=6.04q^{-1}-6.04q^{-2}$

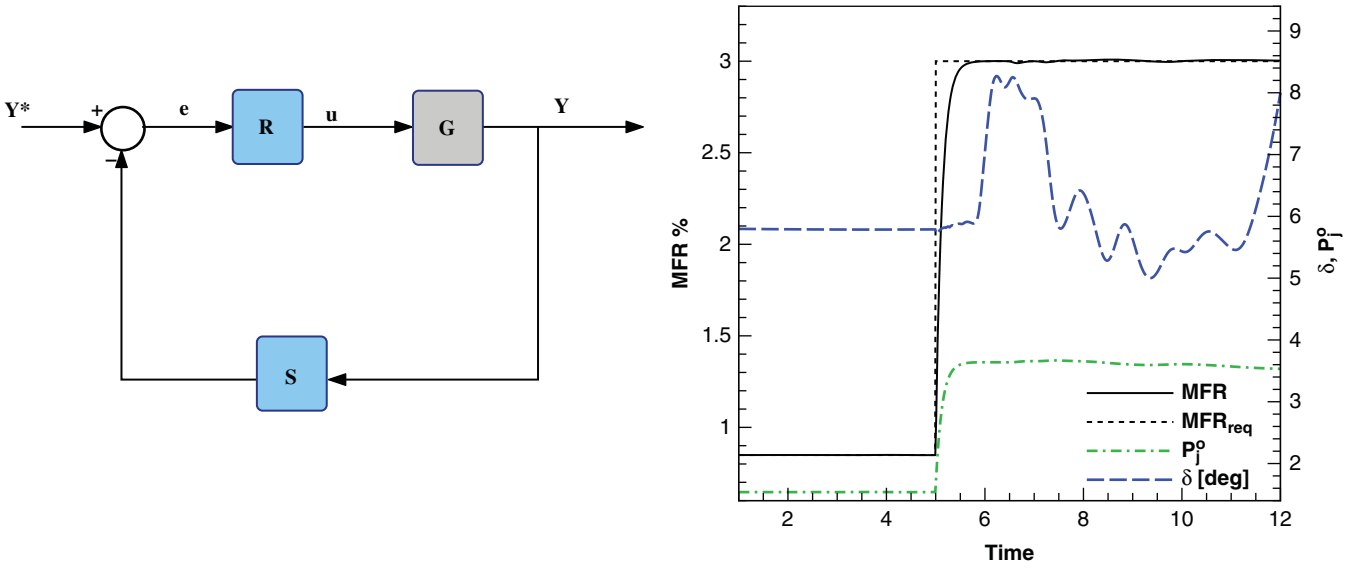

Fig. 16 Sketch of the closed-loop control of the nozzle system (left) and the plot of the system response under PID control (right) with required output $Y^* = \mathrm{MFR}_{\mathrm{req}}(t)$, actual output $Y = \mathrm{MFR}(t)$, and $u(t) = P_j^o(t)$.

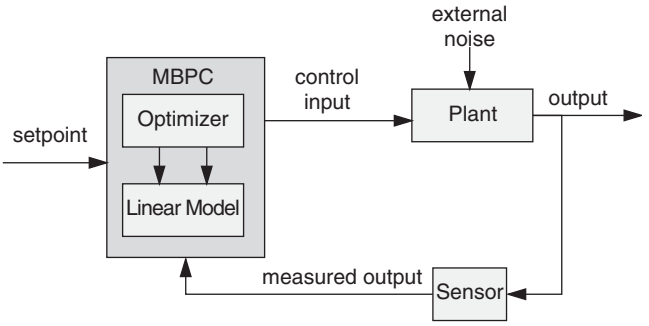

Fig. 17 MPC system diagram including the model predictive controller.

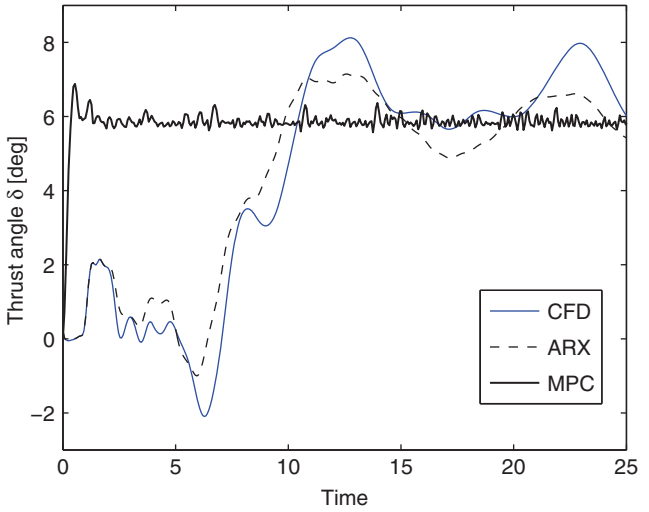

Fig. 18 Model-based predictive control for Case-5 with plant mismatch and external noise.

limiting values of the both the control action u and system response y. For instance, in our case,

$$u_{\min} \le u(t) \le u_{\max}, \qquad \Delta u_{\min} \le u(t) - u(t-1) \le \Delta u_{\max},$$
$$y_{\min} \le y(t) \le y_{\max}, \qquad \forall\, t > 0 \tag{20}$$

Standard methods of solution of the proposed problem, as the direct matrix control, can be found in reference textbooks such as [31]. In Fig. 18, a numerical experiment of the MPC closed-loop control for case 5 is presented. The ARX model is used for deriving the control action as well as for computing the system dynamics. Plant mismatch and white noise in input have been also added [31]. As visible in Fig. 18, the resulting closed-loop dynamics appears very fast, if compared with the open-loop dynamics computed either by CFD or by the linear model. Moreover, we may observe that this result has been obtained in the limit of infinitely fast dynamics of sensors and actuators. As explained in previous sections, this represents the worst case. By taking into account realistic models of sensors and actuators, a slower response of the system is expected that makes the control easier.

V. Conclusions

A computational technique based on the compressible URANS equations has been employed to investigate the dynamic response of a dual-throat nozzle in open- and closed-loop control. The numerical method was previously validated for the supersonic DTN tested at NASA Langley Research Center [6,19]. Nozzle performances and thrust-vector angles were computed for a wide range of nozzle pressure ratios and secondary flow injection rates. The numerical results [19] were in good agreement with the experimental data available in the open literature.

This nozzle concept enhances the thrust-vectoring efficiency of the throat skewing method by generating a cavity flow system downstream of the nozzle throat that maximizes the pressure differentials between the upper and lower wall. As a drawback, the DTN flowfield is characterized by a complex and nonlinear dynamic response caused by the strong interactions between moving shocks, boundary layers, and separated flow regions. These phenomena have been investigated numerically in the present paper by fully unsteady CFD computations including the control system. Several computations of the open-loop dynamics of the nozzle under different forcing have been performed to investigate the system response in terms of thrust-vectoring effectiveness and controllability. We observed that the DTN nozzle system exhibits a typical behavior to step forcing. A flicklike phenomenon in the thrust angle appears from this CFD analysis. After the step input, an initial trend-following response is observed, followed by an abrupt undershoot and then by a new trend-following phase. Finally, the target thrust angle is reached with a series of damped oscillations. As confirmed by CFD and experimental investigations, the system remains stable for a wide range of secondary blowing ratios. Moreover, the system response behaves smoothly if a slow-varying input forcing (e.g., a ramp input) is used or

when the actuator dynamics is introduced, but this behavior was not observed in all the simulated operating conditions. For instance, the overshoots and undershoots still appear when the system is started from the neutral configuration ($\delta = 0$). The closed-loop simulations we performed have put on evidence difficulties in controlling the thrust angle by using pure PID control actions, whereas there are other variables such as, for instance, the MFR, easily controllable even by a simple PID regulator. The computations of the nozzle open-loop dynamics have been used to extract linear ARX models. The closed-loop model predictive control of the nozzle system, based on these ARX models, has been successfully addressed. The wide range of investigations carried out in the present work has revealed useful information about the DTN system response and the possible strategies of the nozzle control for fluidic thrust vectoring.

Acknowledgment

Computational resources were provided by HPC@POLITO, a project of Academic Computing within the Department of Control and Computer Engineering at the Politecnico di Torino (http://www.hpc.polito.it).

References

[1] Asbury, S., and Capone, F., "High-Alpha Vectoring Characteristics of the F-18/HARV," *Journal of Propulsion and Power*, Vol. 10, No. 1, 1994, pp. 116–121. doi:10.2514/3.23719

[2] Wilde, P., Crowther, W., Buonanno, A., and Savvaris, A., "Aircraft Control Using Fluidic Maneuver Effectors," *26th AIAA Applied Aerodynamics Conference*, AIAA Paper 2008-6406, Aug. 2008.

[3] Mason, M., and Crowther, W., "Fluidic Thrust Vectoring for Low Observable Air Vehicles," *2nd AIAA Flow Control Conference*, AIAA Paper 2004-2210, June–July 2004.

[4] Deere, K., "Summary of Fluidic Thrust Vectoring Research Conducted at NASA Langley Research Center," *21st AIAA Applied Aerodynamics Conference*, AIAA Paper 2003-3800, 2003, http://ntrs.nasa.gov/archive/nasa/casi.ntrs.nasa.gov/20030062131.pdf.

[5] Deere, K., Berrier, B., Flamm, J., and Johnson, S., "A Computational Study of a New Dual Throat Fluidic Thrust Vectoring Nozzle Concept," AIAA Paper 2005-3502, July 2005.

[6] Flamm, J., Deere, K., Mason, M., Berrier, B., and Johnson, S., "Design Enhancements of the Two-Dimensional, Dual Throat Fluidic Thrust Vectoring Nozzle Concept," *3rd AIAA Flow Control Conference*, AIAA Paper 2006-3701, June 2006.

[7] Deere, K., Flamm, J., Berrier, B., and Johnson, S., "Computational Study of an Axisymmetric Dual Throat Fluidic Thrust Vectoring Nozzle for a Supersonic Aircraft Application," *43rd AIAA/ASME/SAE/ASEE Joint Propulsion Conference & Exhibit*, AIAA Paper 2007-5085, July 2007.

[8] Balu, R., Marathe, A., Paul, P., and Mukunda, H., "Analysis of Performance of a Hot Gas Injection Thrust Vector Control System," *Journal of Propulsion and Power*, Vol. 7, No. 4, 1991, pp. 580–585. doi:10.2514/3.23365

[9] Yagle, P., Miller, D., Ginn, K., and Hamstra, J., "Demonstration of Fluidic Throat Skewing for Thrust Vectoring in Structurally Fixed Nozzles," *ASME Journal of Engineering for Gas Turbines and Power*, Vol. 123, No. 3, 2001, pp. 502–507. doi:10.1115/1.1361109

[10] Deng, R., and Kim, H. D., "A Study on the Thrust Vector Control Using a Bypass Flow Passage," *Proceedings of the Institution of Mechanical Engineers, Part G: Journal of Aerospace Engineering*, Vol. 229, No. 9, 2015, pp. 1722–1729.

[11] Flamm, J., Deere, K., Mason, M., Berrier, B., and Johnson, S., "Experimental Study of an Axisymmetric Dual Throat Fluidic Thrust Vectoring Nozzle for a Supersonic Aircraft Application," *43rd AIAA/ASME/SAE/ASEE Joint Propulsion Conference & Exhibit*, AIAA Paper 2007-5084, July 2007.

[12] Bellandi, E., and Slippey, A., "Preliminary Analysis and Design Enhancements of a Dual-Throat FTV Nozzle Concept," *39th AIAA Fluid Dynamics Conference*, AIAA Paper 2009-3900, June 2009.

[13] Shin, C., Kim, H., Setoguchi, T., and Matsuo, S., "A Computational Study of Thrust Vectoring Control Using Dual Throat Nozzle," *Journal of Thermal Science*, Vol. 19, No. 6, 2010, pp. 486–490. doi:10.1007/s11630-010-0413-x

[14] Gu, R., Xu, J., and Guo, S., "Experimental and Numerical Investigations of a Bypass Dual Throat Nozzle," *ASME Journal of Engineering for Gas Turbines and Power*, Vol. 136, No. 8, 2014, Paper 084501. doi:10.1115/1.4026943

[15] Eilers, S., Wilson, M., Whitmore, S., and Peterson, Z., "Side Force Amplification on an Aerodynamically Thrust Vectored Aerospike Nozzle," *Journal of Propulsion and Power*, Vol. 28, No. 4, 2012, pp. 811–819. doi:10.2514/1.B34381

[16] Guo, D., Cary, A., and Agarwal, R., "Numerical Simulation of Vectoring of a Primary Jet with a Synthetic Jet," *AIAA Journal*, Vol. 41, No. 12, 2003, pp. 2364–2370. doi:10.2514/2.6861

[17] Gonzalez, D., Gaitondeb, D., and Lewisc, M., "Large-Eddy Simulations of Plasma-Based Asymmetric Control of Supersonic Round Jets," *International Journal of Computational Fluid Dynamics*, Vol. 29, Nos. 3–5, 2015, pp. 240–256. doi:10.1080/10618562.2015.1053877

[18] Gu, R., and Xu, J., "Dynamic Experimental Investigations of a Bypass Dual Throat Nozzle," *ASME Journal Engineering for Gas Turbines and Power*, Vol. 137, No. 8, 2015, Paper 084501. doi:10.1115/1.4029391

[19] Ferlauto, M., and Marsilio, R., "A Numerical Method for the Study of Fluidic Thrust-Vectoring," *Advances in Aircraft and Spacecraft Science*, Vol. 3, No. 4, 2016, pp. 367–378. doi:10.12989/aas.2016.3.4.367

[20] Spalart, P., and Allmaras, S., "A One-Equation Turbulence Model for Aerodynamic Flows," *La Recherche Aerospatiale*, Vol. 1, 1994, pp. 5–21.

[21] Spalart, P., Johnson, F., and Allmaras, S., "Modifications and Clarifications for the Implementation of the Spalart–Allmaras Turbulence Model," *Proceedings of the 7th International Conference on Computational Fluid Dynamics (ICCFD7)*, Paper ICCFD7-1902, Big Island, HA, 2012, http://www.iccfd.org/iccfd7/assets/pdf/papers/ICCFD7-1902_paper.pdf.

[22] Ferlauto, M., and Marsilio, R., "A Computational Approach to the Simulation of Controlled Flows by Synthetic Jets Actuators," *Advances in Aircraft and Spacecraft Science*, Vol. 2, No. 1, 2014, pp. 77–94. doi:10.12989/aas.2015.2.1.077

[23] Vatsa, V., and Turkel, E., "Simulation of Synthetic Jets Using Unsteady Reynolds-Averaged Navier–Stokes Equations," *AIAA Journal*, Vol. 44, No. 2, 2006, pp. 217–224. doi:10.2514/1.13535

[24] Ferlauto, M., and Marsilio, R., "Computation of Plug Nozzle Turbulent Flowfields," *15th AIAA/ISOABE International Symposium on Air-breathing Engines*, edited by Waltrup, P. J., ISABE Paper 2001-1185, Bangalore, India, Sept. 2001.

[25] Ferlauto, M., and Rosa Taddei, S., "Reduced Order Modelling of Full-Span Rotating Stall for the Flow Control Simulation of Axial Compressors," *Proceedings of the Institution of Mechanical Engineering, Part A: Journal of Power and Energy*, Vol. 229, No. 4, 2015, pp. 359–366.

[26] Ferlauto, M., and Marsilio, R., "A Viscous Inverse Method for Aerodynamic Design," *Computer and Fluids*, Vol. 35, No. 3, 2006, pp. 304–325. doi:10.1016/J.COMPFLUID.2005.01.003

[27] Ferlauto, M., "A Pseudo-Compressibility Method for Solving Inverse Problems Based on the 3D Incompressible Euler Equations," *Inverse Problems in Science and Engineering*, Vol. 23, No. 5, 2015, pp. 798–817. doi:10.1080/17415977.2014.939653

[28] Poinsot, T., and Lele, S., "Boundary Conditions for Direct Simulations of Compressible Viscous Reacting Flows," *Journal of Computational Physics*, Vol. 101, No. 1, 1992, pp. 104–129. doi:10.1016/0021-9991(92)90046-2

[29] Ferlauto, M., Iollo, A., and Zannetti, L., "Set of Boundary Conditions for Aerodynamic Design," *AIAA Journal*, Vol. 42, No. 8, 2004, pp. 1582–1592. doi:10.2514/1.2340

[30] Ljung, L., *System Identification, Theory for the Use*, Prentice–Hall, Upper Saddle River, NJ, 1987.

[31] Camacho, E., and Bordons, C., *Model Predictive Control*, Springer–Verlag, Berlin, 2004.

[32] Ziegler, J., and Nichols, N., "Optimum Settings for Automatic Controllers," *Transactions of the ASME*, Vol. 64, Nov. 1942, pp. 759–768.

[33] Huang, S., and Kim, J., "Control and System Identification of a Separated Flow," *Physics of Fluids*, Vol. 20, No. 10, 2008, Paper 101509.

S. Fu
Associate Editor